Fluid Phase Equilibria 589 (2025) 114260

Contents lists available at ScienceDirect

Fluid Phase Equilibria

journal homepage: www.journals.elsevier.com/fluid-phase-equilibria

How reliable is the Real Adsorbed Solution Theory (RAST) for estimating ternary mixture equilibrium in microporous host materials?

Rajamani Krishna *, Jasper M. van Baten

Van 't Hoff Institute for Molecular Sciences, University of Amsterdam, Science Park 904, 1098 XH Amsterdam, the Netherlands

ARTICLE INFO

Keywords:
CO_2 capture
Cation-exchanged zeolites
Thermodynamic non-idealities
Segregated adsorption
Hydrogen bonding
Activity coefficients

ABSTRACT

Microporous crystalline adsorbents such as zeolites, and metal-organic frameworks (MOFs) have potential use in a wide variety of separations applications. In applications such as CO_2 capture, the Ideal Adsorbed Solution Theory (IAST) often fails to provide a quantitative description of mixture adsorption equilibrium especially in cation-exchanged zeolites. The failure of the IAST is ascribable to non-compliance with one or more tenets mandated by the IAST such as (a) homogeneous distribution of adsorbates within the pore landscape, (b) no preferential location of guest species, and (c) absence of molecular clustering due to say hydrogen bonding. The focus of this article is on the reliability of the Real Adsorbed Solution Theory (RAST) models for quantitative estimation of adsorption equilibrium. Configurational-Bias Monte Carlo (CBMC) simulations are undertaken to determine the adsorption equilibrium for ternary $CO_2/CH_4/N_2$, $CO_2/CH_4/C_3H_8$, $CO_2/CH_4/H_2$, and water/methanol/ethanol mixtures in NaX, LTA-4A, CHA, DDR, and MFI zeolites. Additionally, CBMC simulations of the constituent binary pairs are used to determine the Wilson or NRTL parameters, taking due account of the dependence of the activity coefficients on the spreading pressure. Use of the binary pair Wilson or NRTL parameters allows the estimation of ternary mixture adsorption equilibrium, that is tested against the CBMC data on component loadings. In all investigated guest/host combinations, the RAST provides a good estimation of ternary mixture adsorption equilibrium.

1. Introduction

Microporous adsorbents such as zeolites, and metal-organic frameworks (MOFs) offer energy-efficient alternatives to conventional separation technologies such as distillation. There has been a tremendous upsurge in research on the development of MOFs for a variety of applications such as CO_2 capture, alkene/alkane, alkyne/alkene, water/alcohol mixture separations. For n-component mixture adsorption, the selectivity of guest constituent i with respect to another guest constituent j, in that mixture, $S_{ads,ij}$, is defined by

$$S_{ads,ij} = \frac{q_i/q_j}{f_i/f_j} = \frac{q_i/q_j}{y_i/y_j} \tag{1}$$

where q_i, q_j are the molar loadings of the constituents i and j, in the adsorbed phase in equilibrium with the bulk fluid phase mixture having partial fugacities f_i, f_j and mole fractions in the bulk phase mixture $y_i = f_i/f_t; \quad f_t = \left(\sum_{k=1}^{n} f_k\right)$. For estimation of the component loadings and selectivity, $S_{ads,ij}$, it is common practice to use the Ideal Adsorbed Solution Theory (IAST) [1,2] that requires the unary isotherm data as inputs.

The Myers-Prausnitz development of the IAST [1] is based on the analog of Raoult's law for vapor-liquid equilibrium, i.e.

$$f_i = P_i^0 x_i; \quad i = 1, 2, \ldots n \tag{2}$$

where x_i are the mole fractions in the adsorbed phase mixture

$$x_i = q_i/q_t; \quad q_t = q_1 + q_2 + \ldots + q_n; \quad i = 1, 2, \ldots n \tag{3}$$

and P_i^0 is the pressure for sorption of every component i, which yields the same spreading pressure, π, for each of the pure components, as that for the mixture:

$$\frac{\pi A}{RT} = \int_0^{P_1^0} \frac{q_1^0(f)}{f} df = \int_0^{P_2^0} \frac{q_2^0(f)}{f} df = \int_0^{P_3^0} \frac{q_3^0(f)}{f} df = \ldots \tag{4}$$

In Eq. (4), A represents the surface area per kg of framework, and $q_i^0(f)$ is the *pure* component adsorption isotherm; the superscript 0 is

* Corresponding author.
E-mail addresses: r.krishna@uva.nl, r.krishna@contact.uva.nl (R. Krishna).

https://doi.org/10.1016/j.fluid.2024.114260
Received 31 July 2024; Received in revised form 14 October 2024; Accepted 19 October 2024
Available online 20 October 2024
0378-3812/© 2024 The Author(s). Published by Elsevier B.V. This is an open access article under the CC BY license (http://creativecommons.org/licenses/by/4.0/).

Nomenclature

Latin alphabet

A	surface area per kg of framework, m^2 kg^{-1}
C	constant used in Eqs. (11) and (13), kg mol^{-1}
f_i	partial fugacity of species i, Pa
f_t	total fugacity of bulk fluid mixture, Pa
G^{ex}	excess Gibbs free energy, J mol^{-1}
G_{ij}	NRTL parameters, dimensionless
n	number of species in the mixture, dimensionless
P_i^0	sorption pressure, Pa
q_i	molar loading of species i, mol kg^{-1}
$q_i^0(f)$	pure component adsorption isotherm for i, mol kg^{-1}
q_t	total molar loading of mixture, mol kg^{-1}
$q_{sat,mix}$	saturation capacity of mixture, mol kg^{-1}
R	gas constant, 8.314 J mol^{-1} K^{-1}
S_{ads}	adsorption selectivity, dimensionless
T	absolute temperature, K
x_i	mole fraction of species i in adsorbed phase, dimensionless
y_i	mole fraction of species i in bulk fluid mixture, dimensionless

Greek alphabet

α	NRTL parameters, dimensionless
γ_i	activity coefficient of component i in adsorbed phase, dimensionless
Λ_{ij}	Wilson parameters, dimensionless
θ	fractional occupancy, dimensionless
π	spreading pressure, N m^{-1}
Φ	surface potential, mol kg^{-1}

Subscripts

i,j	components in mixture
t	referring to total mixture
sat	referring to saturation conditions

Superscripts

0	referring to pure component loading
ex	referring to excess parameter

used to emphasize that $q_i^0(f)$ relates the *pure component* loading to the bulk fluid fugacity. Since the surface area A is not directly accessible from experimental data, the surface potential, [3,4] $\frac{\pi A}{RT} \equiv \Phi$, with the units mol kg^{-1}, serves as a convenient and practical proxy for the spreading pressure, π [3,5-7].

For multicomponent mixture adsorption, each of the equalities on the right side of Eq. (4) must be satisfied. These constraints may be solved using a suitable equation solver, to yield the set of values of P_1^0, P_2^0, P_3^0,..P_n^0, all of which satisfy Eq. (4). The corresponding values of the integrals using the P_i^0 as upper limits of integration must yield the same value of the surface potential Φ for each component; this ensures that the obtained solution is the correct one.

The adsorbed phase mole fractions x_i are then determined from

$$x_i = f_i \,/\, P_i^0; \quad i = 1, 2, ...n \tag{5}$$

The applicability of Eq. (5) mandates that all of the adsorption sites within the microporous material are equally accessible to each of the guest molecules, implying a homogeneous distribution of guest adsorbates within the pore landscape, with no preferential locations of any guest species.

In view of Eqs. (3), and (5), we re-write Eq. (1), as the ratio of the sorption pressures

$$S_{ads,ij} = P_j^0 \,\Big/\, P_i^0 \tag{6}$$

Applying the restriction specified by Eq. (4), it follows that $S_{ads,ij}$ is uniquely determined by the surface potential Φ; this has been established for a large number of guest/host combinations [7,8]. It is important to note that Eq. (6) is valid irrespective of the total number of components in the mixture. Put another way, the presence of component 3 in the ternary mixture has no *direct* influence of the adsorption selectivity $S_{ads,12} = P_2^0 / P_1^0$ for the 1–2 pair, except for the fact that the surface potential Φ that satisfies Eq. (4) is altered due to presence of component 3.

A further key assumption of the IAST is that the adsorption enthalpies and surface areas of the adsorbed molecules do not change upon mixing with other guests. If the total mixture loading is q_t, the area covered by the adsorbed mixture is $\frac{A}{q_t}$ with units of m^2 (mole mixture)$^{-1}$. Therefore, the assumption of no surface area change due to mixture adsorption translates as $\frac{A}{q_t} = \frac{Ax_1}{q_1^0(P_1^0)} + \frac{Ax_2}{q_2^0(P_2^0)} + \cdots \frac{Ax_n}{q_n^0(P_n^0)}$; the total mixture loading is $q_t = q_1 + q_2 ... + q_n$ is calculated from

$$\frac{1}{q_t} = \frac{x_1}{q_1^0(P_1^0)} + \frac{x_2}{q_2^0(P_2^0)} + ... + \frac{x_n}{q_n^0(P_n^0)} \tag{7}$$

in which $q_1^0(P_1^0)$, $q_2^0(P_2^0)$,... $q_n^0(P_n^0)$ are determined from the unary isotherm fits, using the sorption pressures for each component P_1^0, P_2^0, P_3^0,..P_n^0, that are available from the solutions to Eq. (4). The occurrence of molecular clustering and hydrogen bonding should be expected to invalidate the applicability of Eq. (7) because the surface area occupied by a molecular cluster is different from that of each of the un-clustered guest molecules in the adsorbed phase.

The ratio of the total mixture loading, q_t, to the saturation capacity of the mixture, $q_{sat,mix}$ is the fractional pore occupancy, θ, that is relatable to Φ as follows (see the SI for complete derivation)

$$\theta \equiv q_t \,/\, q_{sat,mix} = 1 - \exp\left(-\Phi \,/\, q_{sat,mix}\right) \tag{8}$$

where the saturation capacity $q_{sat,mix}$ may be estimated from the saturation capacities of the constituent guests

$$\frac{1}{q_{sat,mix}} = \sum_{k=1}^{n} \frac{x_k}{q_{k,sat}} \tag{9}$$

The surface potential Φ is therefore also interpretable as a proxy for the pore occupancy, θ.

Despite the widespread usage of the IAST, a limited number of experimental investigations have found that IAST estimates of component loadings for mixture adsorption are not in quantitative agreement with experimental data. These studies include adsorption of binary CO_2/N_2 [9,10], CO_2/CH_4, [4,10-13], CO_2/C_3H_8 [3,14-16], CO_2/C_2H_4

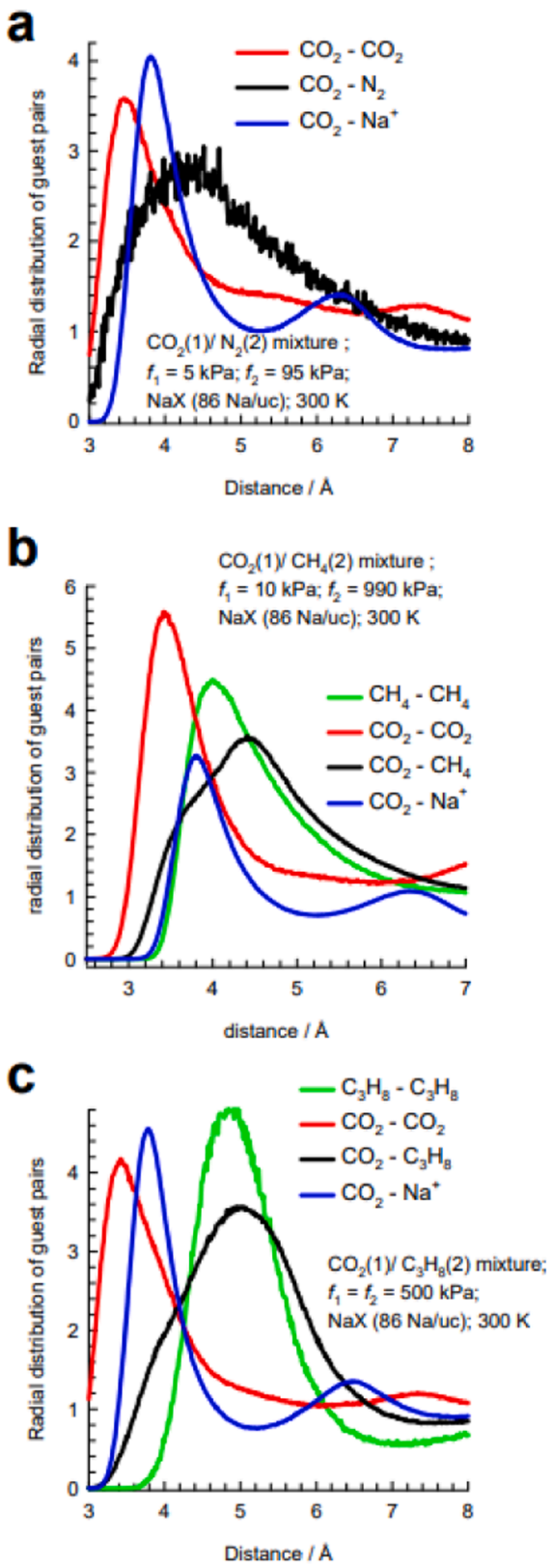

Fig. 1. Radial distribution of guest pairs determined from CBMC simulations for adsorption of (a) CO_2/N_2, (b) CO_2/CH_4, and (c) CO_2/C_3H_8 mixtures in NaX zeolite (106 Si, 86 Al, 86 Na^+, Si/Al=1.23) at 300 K. The samples were taken up to a radial distance of 12 Å, but the *x*-axis has been truncated at 8 Å because only the first peaks are of interest in the discussions. All simulation details are provided in the Supplementary Material accompanying this publication.

[17-20], C_2H_4/iso-C_4H_{10} [21], CO_2/H_2S [16], and H_2S/C_3H_8 [16] mixtures in cation-exchanged zeolites such as NaX (commonly known by its trade name 13X), LTA-4A, LTA-5A, H-ZSM-5, and H-MOR. Experimental data on adsorption of water/alcohol mixtures clearly demonstrate the failure of the IAST for variety of host materials [22-26]. A limited number of experimental studies report the failure of the IAST for ternary mixtures: $CO_2/CH_4/N_2$ in NaX [10], $CO_2/C_2H_4/C_2H_6$ in NaX [3], $CO_2/C_2H_4/C_3H_8$ in NaX [14], $CO_2/C_3H_6/C_3H_8$ in NaX [14], $CO_2/C_2H_4/C_3H_8$ in HZSM-5, and $CO_2/H_2S/C_3H_8$ in H-MOR [16]. A detailed RAST analysis of published experimental data is provided in Figures S113 – S147.

Noteworthily, the analyses of the cited experimental studies have often included Real Adsorbed Solution Theory (RAST) models for the activity coefficients, γ_i, determined from

$$\gamma_i = \frac{f_i}{P_i^0 x_i} \tag{10}$$

Unlike the description of non-idealities in bulk fluid phase mixtures, models for the activity coefficients, γ_i, in the adsorbed phase must include the dependence of γ_i on the pore occupancy. For example, the Wilson model for adsorption of *n*-component mixtures is described by a set of parameters Λ_{ij}; C

$$\ln(\gamma_i) = \left(1 - \ln\left(\sum_{j=1}^{n} x_j \Lambda_{ij}\right) - \sum_{k=1}^{n} x_k \frac{\Lambda_{ki}}{\sum_{l=1}^{n} x_l \Lambda_{kl}}\right)(1 - \exp(-C\Phi)); \quad \Lambda_{ii} \equiv 1; \quad i = 1, 2, \ldots n \tag{11}$$

The inclusion of the correction factor $(1-\exp(-C\Phi))$ imparts the correct limiting behaviors for the activity coefficients in the Henry regime at vanishingly small pore occupancies

$$\Phi \to 0; \quad \theta \to 0; \quad \gamma_i \to 1 \tag{12}$$

Our earlier works [26-28] have underscored the need for including the correction factor $(1-\exp(-C\Phi))$ in RAST modelling, though this correction is often ignored in many published works [29-32].

A comparison of Eqs. (8), (9), and (11) shows that the factor C may well be identified with the inverse of the saturation capacity of *n*-component mixture $q_{sat,mix}$. Therefore, it is possible to make estimates of the parameter C, by using the unary isotherm fits to determine the saturation capacities of each component, $q_{i,sat}$; more detailed discussions are provided in the Supplementary Material accompanying this article.

The corresponding NRTL model for activity coefficients is

$$\ln(\gamma_i) = \left[\frac{\sum_{j=1}^{n} x_j \tau_{ji} G_{ji}}{\sum_{k=1}^{n} x_k G_{ki}} + \sum_{j=1}^{n} \frac{x_j G_{ij}}{\sum_{k=1}^{n} x_k G_{kj}}\left(\tau_{ij} - \frac{\sum_{l=1}^{n} x_l \tau_{lj} G_{lj}}{\sum_{k=1}^{n} x_k G_{kj}}\right)\right](1 - \exp(-C\Phi))$$

$$G_{ij} = \exp(-\alpha_{ij}\tau_{ij}); \quad \alpha_{ij} = \alpha_{ji}; \quad \tau_{ii} = 0; \quad G_{ii} = 1 \tag{13}$$

For calculation of the total mixture loading we need to replace Eq. (7) by

$$\frac{1}{q_t} = \sum_{i=1}^{n} \frac{x_i}{q_i^0(P_i^0)} + \left.\frac{\partial(G^{ex}/RT)}{\partial\Phi}\right|_{T,x} \tag{14}$$

With the introduction of activity coefficients, the expression for the adsorption selectivity for the *i-j* pair in an *n*-component mixture is

$$S_{ads,ij} = \frac{q_i/q_j}{f_i/f_j} = \frac{x_i/x_j}{f_i/f_j} = \frac{P_j^0 \gamma_j}{P_i^0 \gamma_i} \tag{15}$$

Since the activity coefficients are composition dependent, the adsorption selectivity is also composition dependent, and S_{ads} is not

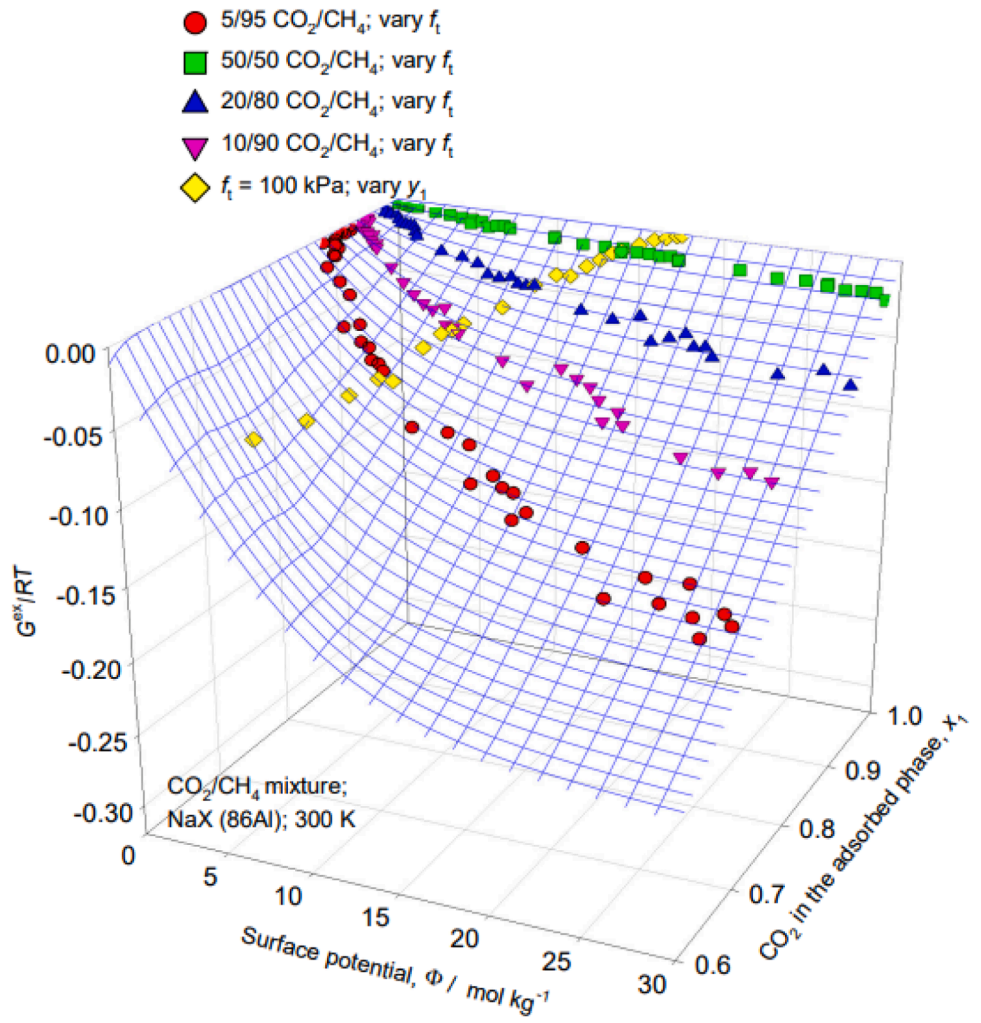

Fig. 2. 3D plots of CBMC data on excess Gibbs free energy G^{ex}/RT for $CO_2(1)/CH_4(2)$ mixture adsorption in NaX zeolite at 300 K, plotted as function of the surface potential, Φ, and the mole fraction of CO_2 in the adsorbed phase mixture, x_1. The 3D mesh is constructed using the Wilson parameters provided in Table S10. All simulation details are provided in the Supplementary Material accompanying this publication.

uniquely related to the surface potential, Φ, as is the case for the IAST.

The key question addressed in this article is: Is it possible to make good estimates of adsorption equilibrium in ternary mixtures using as inputs data on the RAST models for the constituent binary pairs of guest molecules? To address this query, we resort to Configurational-Bias Monte Carlo (CBMC) simulations of the ternary mixture adsorption equilibrium for $CO_2/CH_4/N_2$, $CO_2/CH_4/C_3H_8$, $CO_2/CH_4/H_2$, and water/methanol/ethanol mixtures in five different host materials: NaX, LTA-4A, CHA, DDR, and MFI zeolites. In each case, CBMC data were also determined for the constituent binary pairs in order to determine the appropriate Wilson or NRTL parameters for modeling the activity coefficients. The CBMC simulations are performed using the methodology that is firmly established in the literature [33-35]; details are provided in the Supplementary Material accompanying this publication, that also provides (a) structural details of host zeolites, (b) details of the CBMC simulation methodology including choice of force fields, (b) details of the IAST, and RAST calculations for mixture adsorption equilibrium, (c) unary isotherm fit parameters, (d) Wilson/NRTL parameters fits for thermodynamic non-idealities, (e) plots of CBMC simulation data and comparisons with IAST/RAST estimates, and (f) RAST analysis of published experimental data on mixture adsorption.

2. Inhomogeneous distribution of guests in NaX zeolite

NaX zeolite is the benchmark adsorbent for post-combustion CO_2 capture, with the ability to meet the U.S. Department of Energy (US-DOE) targets for CO_2 purity and recovery [9]. NaX is a Na^+ cation exchanged FAU (= faujasite) zeolite with cages of 786 $Å^3$vol, separated by 7.4 Å 12-ring windows. Per unit cell of NaX zeolite we have 106 Si, 86 Al, 86 Na^+ with Si/Al=1.23. This material is also commonly referred to by its trade name: 13X zeolite. The failure of the IAST to provide a quantitative description of mixture adsorption in NaX zeolite, as reported in several experimental studies [3,4,9-14] is traceable to the use of Raoult's law analog, Eq. (2), whose applicability mandates that all of

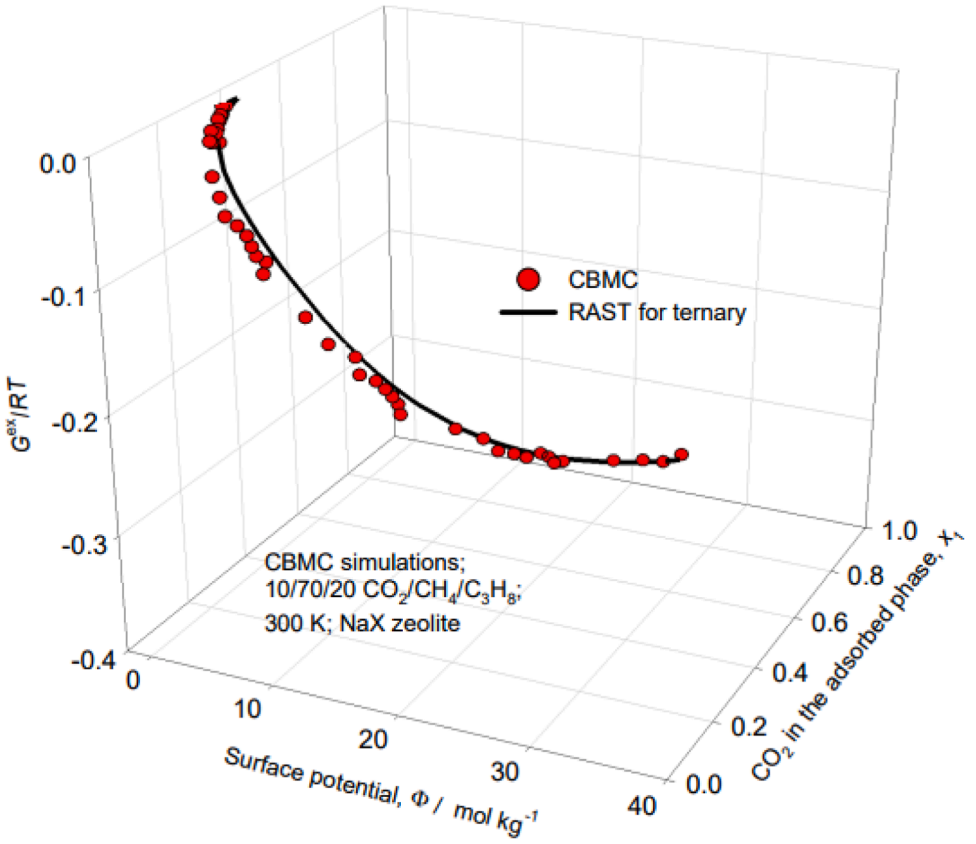

Fig. 3. 3D plot of CBMC data on excess Gibbs free energy G^{ex}/RT for 10/70/20 $CO_2(1)//CH_4(2)/C_3H_8(3)$ mixtures in NaX zeolite at 300 K. Comparison is made of CBMC data with the estimates of the ternary Wilson RAST model. The unary isotherm fit parameters and Wilson parameters are provided in Table S10. All simulation details are provided in the Supplementary Material accompanying this publication.

the adsorption sites within the microporous material are equally accessible to each of the guest molecules, implying a homogeneous distribution of guest adsorbates within the pore landscape, with no preferential locations of any guest species. To test this requirement, CBMC simulation data on the spatial locations of the guest molecules were sampled to determine the inter-molecular distances. By sampling a total of 10^5 equilibrated simulation steps, the radial distribution of the separation distances between the various molecular pairs were determined for CO_2/N_2, CO_2/CH_4, and CO_2/C_3H_8 mixtures. The data on the radial distribution functions (RDF) are presented in Fig. 1a,b,c. If we compare the first peaks, it is noteworthy that for all three mixtures, the CO_2–CO_2, and CO_2–Na^+ pairs are close together, indicating that the major proportion of CO_2 congregates around the cations. A further point to note is that the CO_2–N_2, CO_2–CH_4, and CO_2–C_3H_8 separation distances are significantly larger than the corresponding CO_2–CO_2 separation distances. This implies that the partner molecules, N_2, CH_4, and C_3H_8, endure less severe competitive adsorption with CO_2 than is anticipated by the IAST; as a consequent, the IAST over-estimates the values of S_{ads}; see Figures S47 – S62.

For quantifying departures from idealities, Fig. 2 plots CBMC data for the excess Gibbs free energy $G^{ex}/RT = x_1\ln(\gamma_1) + x_2\ln(\gamma_2)$ for CO_2/CH_4 mixture adsorption in NaX zeolite at 300 K. The CBMC data clearly show that G^{ex}/RT depends on both the surface potential, Φ, and mole fraction of CO_2 in the adsorbed phase, x_1. The entire CBMC data set resides on a 3D surface mesh created from the fitted Wilson parameters in Table S10: $C = 0.142$; $\Lambda_{12} = 0$; $\Lambda_{21} = 5.715$. The 3D surface plot clearly shows that $\Phi \to 0$; $\theta \to 0$; $\gamma_i \to 1$; $G^{ex}/RT \to 0$. Also, for a fixed value of the surface potential, Φ, we have the limiting characteristics: $x_i \to 1$; $\gamma_i \to 1$ $G^{ex}/RT \to 0$. An analogous plot for CO_2/C_3H_8 mixture adsorption in NaX zeolite is presented in Figure S54.

CBMC simulations for $CH_4(1)/C_3H_8(2)$ mixtures in NaX (see Figure S57) show that the IAST provides a reasonably good description of adsorption equilibrium, because both alkanes are homogeneously distributed within the pore landscape.

CBMC simulations were carried out for 10/70/20 $CO_2(1)/CH_4(2)/C_3H_8(3)$ mixtures in NaX at 300 K for a range of total fugacities, f_t. In Fig. 3, the excess Gibbs free energy G^{ex}/RT determined from CBMC data are plotted in 3D space as function surface potential, Φ, and mole fraction of CO_2 in the adsorbed phase, x_1. The continuous solid line represents the ternary RAST Wilson calculations, using Eq. (11). The Wilson parameters for the binary pairs $\Lambda_{12}, \Lambda_{21}, \Lambda_{13}, \Lambda_{31}, \Lambda_{23}, \Lambda_{32}$ are taken to be the same as for the corresponding binary pairs as listed in Table S10. Noteworthily, $\Lambda_{23} = 1, \Lambda_{32} = 1$ because the CH_4/C_3H_8 mixtures behave ideally (see Figure S57). Our approach for ternary mixtures is to estimate C as $C = \frac{x_1}{q_{1,sat}} + \frac{x_2}{q_{2,sat}} + \frac{x_3}{q_{3,sat}}$, assuming, $x_1 = x_2 = x_3 = 1/3$. The RAST estimates are in reasonable agreement with the ternary CBMC data set.

In Fig. 4, the excess Gibbs free energy $G^{ex}/RT = \sum_{i=1}^{n} x_i\ln(\gamma_i)$

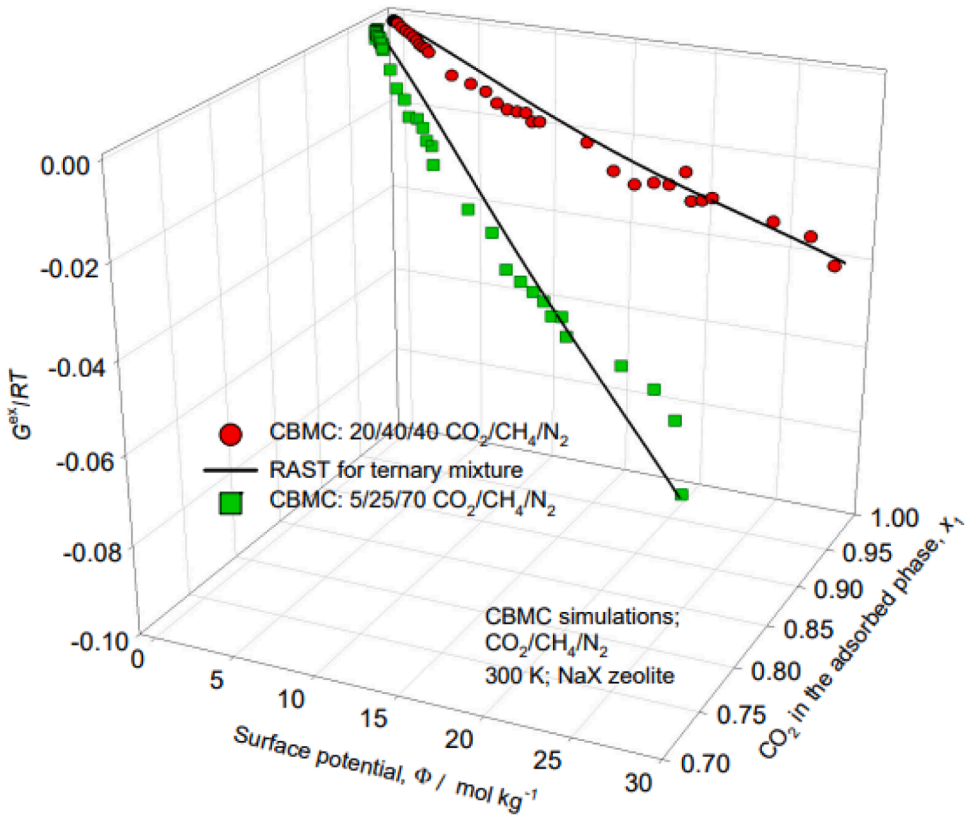

Fig. 4. 3D plot of CBMC data on excess Gibbs free energy G^{ex}/RT for ternary 20/40/40 $CO_2/CH_4/N_2$, and 5/25/70 $CO_2/CH_4/N_2$ mixtures in NaX at 300 K for a range of total fugacities, f_t. Comparison is made of CBMC data with the estimates of the ternary Wilson RAST model. The unary isotherm fit parameters and Wilson parameters are provided in Table S10. All simulation details are provided in the Supplementary Material accompanying this publication.

determined from CBMC data for ternary 20/40/40 $CO_2/CH_4/N_2$, and 5/25/70 $CO_2/CH_4/N_2$ mixtures in NaX for a range of total fugacities, f_t, are plotted in 3D space as function of Φ and x_1. The continuous solid line represents the ternary RAST Wilson calculations using Eq. (11). The Wilson parameters for the binary CO_2/CH_4 and CO_2/N_2 pairs$\Lambda_{12}, \Lambda_{21}, \Lambda_{13}, \Lambda_{31}, \Lambda_{23}, \Lambda_{32}$ are taken to the same as CBMC data for binary pairs as listed in Table S10. Noteworthily, $\Lambda_{23} = 1, \Lambda_{32} = 1$ because the CH_4/N_2 mixtures behave ideally (see Figure S57). The RAST estimates are in good agreement with the two ternary CBMC data sets.

The CBMC data in Figs. 1–4 provide rationalization and quantification of the thermodynamic non-idealities observed in the experimental investigations of CO_2/N_2, CO_2/CH_4, CO_2/C_3H_8, CO_2/C_2H_4, $CO_2/CH_4/N_2$, $CO_2/C_2H_4/C_2H_6$, $CO_2/C_2H_4/C_3H_8$, $CO_2/C_3H_6/C_3H_8$ mixtures in cation exchanged zeolites (NaX, H-ZSM-5, and H-MOR); see Figures S113–S147 [36,37].

2.1. *Preferential perching of CO_2 in window regions*

Zeolites such as LTA-4A, CHA, DDR, and ERI have cages separated by windows with apertures in the 3.6 Å–4.1 Å range [20,38-41]. Due to preferential location (perching) of CO_2 at the windows, the adsorption of CO_2-bearing mixtures exhibits strong thermodynamic non-idealities.

Two different campaigns were carried out for CBMC simulations of $CO_2(1)/C_3H_8(2)$ mixture adsorption in LTA-4A zeolite at 300 K. In campaign A, the mole fraction of $CO_2(1)$ in the bulk gas phase is held constant (at values of $y_1 = 0.1$, and $y_1 = 0.8$), and the bulk gas phase fugacity $f_t = f_1 + f_2$ was varied. In campaign B, the mole fraction of $CO_2(1)$ in the bulk gas phase is held constant, and the bulk gas phase fugacity $f_t = f_1 + f_2$ was varied. The CBMC results of these two campaigns are presented in Fig. 5a,b that compares CBMC data on adsorption selectivity, S_{ads}, with IAST estimates indicated by the dashed lines.

The CBMC data in Fig. 5a for Campaign A show with increasing values of the surface potential Φ, the selectivity S_{ads} becomes increasingly in favor of CO_2, due to strong coulombic interactions with the extra-framework cations Na^+. The IAST anticipates both sets of data to have the same selectivity that depends uniquely on the surface potential Φ, independent of the bulk phase compositions; see Eq. (6). The IAST does not anticipate this selectivity reversal in favor of CO_2, for the CBMC data with $y_1 = 0.1$. The CBMC simulation data show that S_{ads} depends on the bulk gas mixture composition, y_1.

For campaign B, with the bulk gas phase mixture fugacity $f_t = f_1 + f_2 = 1$ MPa we note that the S_{ads} undergoes a selectivity reversal, at $y_1 = 0.1$, that is not anticipated by the IAST; see Fig. 5b.The continuous solid lines in Fig. 5 are the RAST calculations using fitted Wilson parameters as specified in Table S13. Analogous selectivity reversals have been observed in a number of experimental investigations (see Figures S116–S121, S138–S146).

Fig. 6a shows snapshots of the location of $CO_2(1)$, and $C_3H_8(2)$ molecules within the pore topology of LTA-4A zeolite. We note that the CO_2 is almost exclusively located at the windows, or near the window

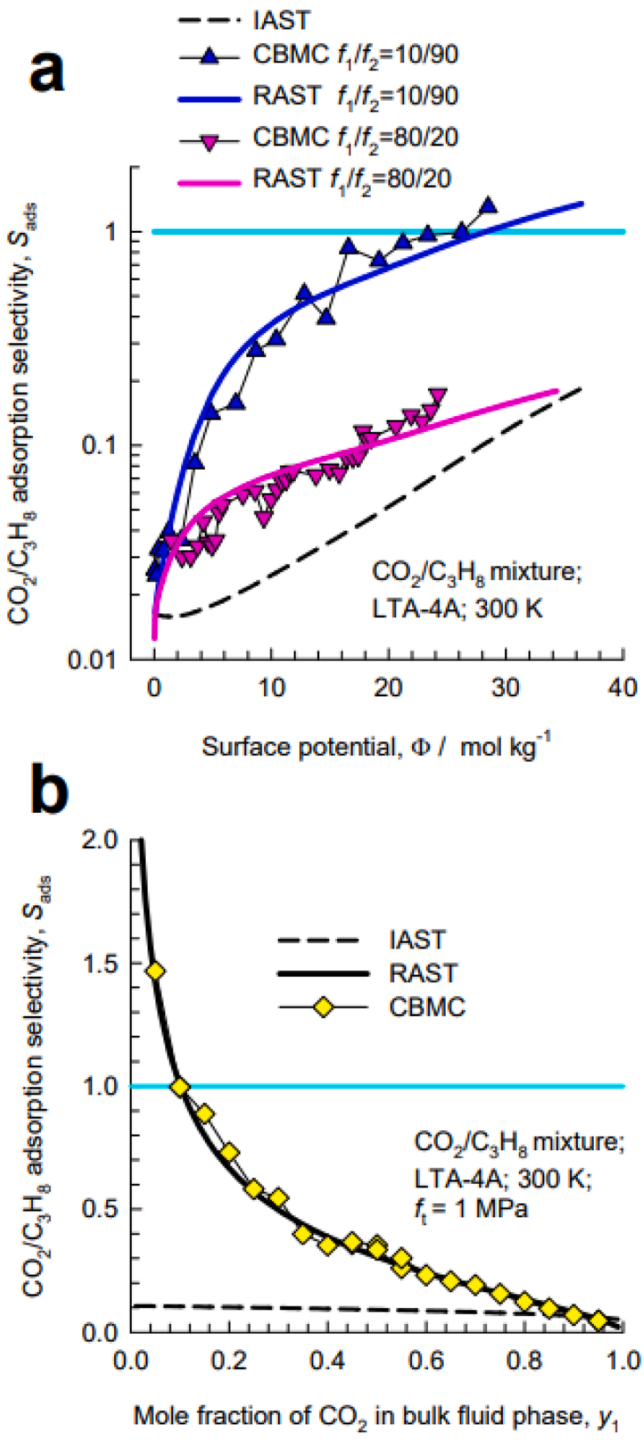

Fig. 5. CBMC simulations data for $CO_2(1)/C_3H_8(2)$ mixture adsorption in LTA-4A zeolite at 300 K. The CBMC data on adsorption selectivity for Campaigns A and B are compared with IAST (dashed lines) and RAST estimates (continuous solid lines). The unary isotherm fit parameters and Wilson parameters are provided in Table S13. All simulation details are provided in the Supplementary Material accompanying this publication.

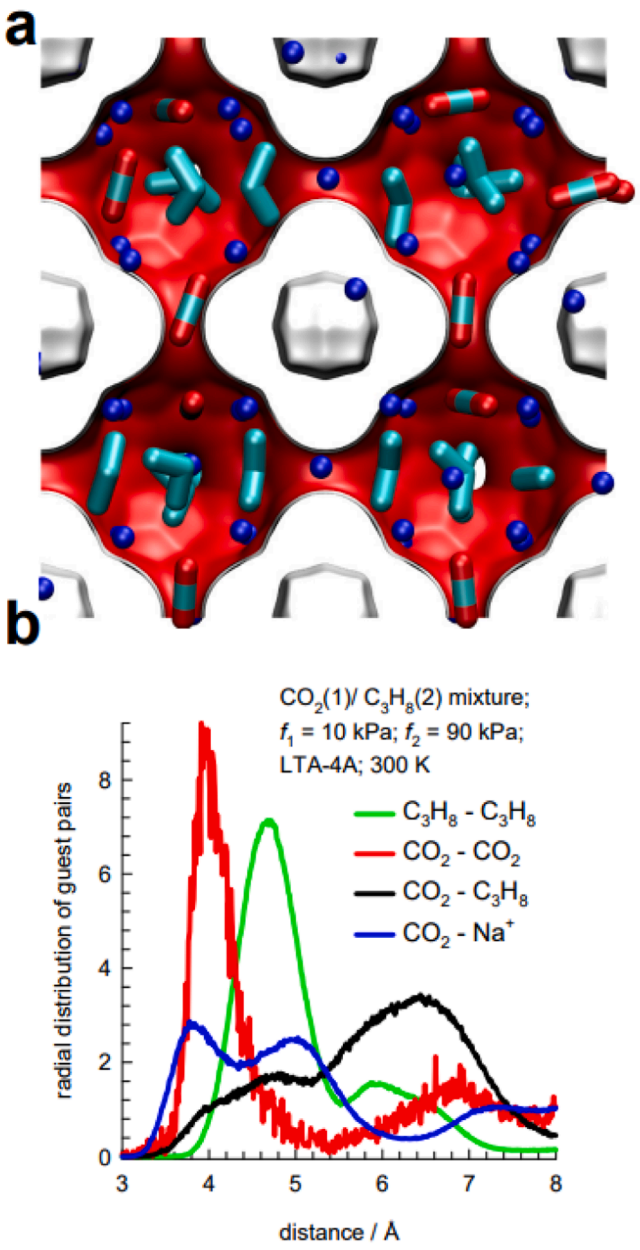

Fig. 6. (a) Computational snapshot showing the location of CO_2, and C_3H_8 within the cages of LTA-4A zeolite at 300 K and total fugacity f_t = 1 MPa. The component partial fugacities are f_1 = 0.8 MPa, and f_2 = 0.2 MPa. (b) Radial distribution of guest pairs determined from CBMC simulations for adsorption of CO_2/C_3H_8 mixtures in LTA-4A zeolite at 300 K and total fugacity f_t = 100 kPa, and y_1=0.1. All simulation details are provided in the Supplementary Material accompanying this publication.

entrance regions, where the extra-framework cations (indicated by blue spheres) are located. Due to configurational restraints, C_3H_8 can only located at the cage interiors. Consequently, the competition between the adsorption of CO_2 and C_3H_8 is less severe than assumed in the homogenous distribution that is inherent in the IAST prescription.

For quantification of the inhomogeneous distribution of guest

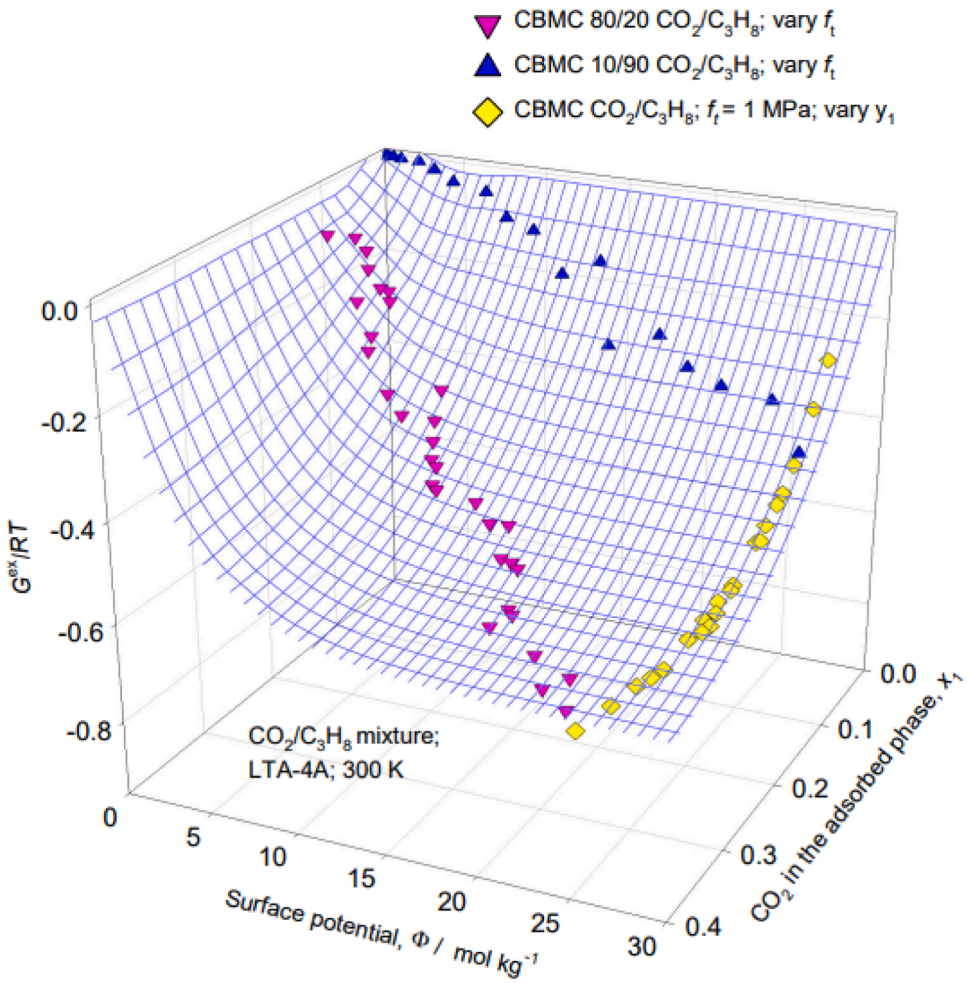

Fig. 7. 3D plots of CBMC data on excess Gibbs free energy G^{ex}/RT for $CO_2(1)/C_3H_8(2)$ mixture adsorption in LTA-4A zeolite at 300 K. The 3D mesh is constructed using the Wilson parameters provided in Table S13. All simulation details are provided in the Supplementary Material accompanying this publication.

adsorbates, Fig. 6b presents the radial distribution functions (RDFs) for various guest pairs CO_2-CO_2, CO_2-Na^+, CO_2-C_3H_8, and C_3H_8-C_3H_8 . It is noteworthy that the first peaks of CO_2-CO_2 and CO_2-Na^+ are close together, confirming the congregation of CO_2 around the Na^+ ions. Also noteworthy is that the first peaks of CO_2-CO_2 and CO_2-C_3H_8 are farther apart, indicating segregation effects.

The transient breakthrough experimental data of van Zandvoort et al. [18,19] demonstrate the phenomenon of selectivity reversals for $CO_2(1)/C_2H_4(2)$ mixture separation in a fixed bed adsorber using in LTA-5A zeolite (see Figure S120 and S121). The selectivity reversal phenomena can be rationalized on the basis of inhomogeneous distribution of guest adsorbates as witnessed in Fig. 6; see [20,42-44]. The RAST modeling of transient breakthroughs is in excellent agreement with experiments; see Figure S121.

In Fig. 7, the CBMC data sets for the excess Gibbs free energy G^{ex}/RT are plotted in 3D space as function of Φ and x_1. The entire CBMC data set resides on a 3D surface mesh determined from the fitted Wilson parameters in Table S13. The 3D surface plot clearly shows that $\Phi \to 0$; $\theta \to 0$; $\gamma_i \to 1$; $G^{ex}/RT \to 0$. Also, for a fixed value of the surface potential, Φ, we have the limiting characteristics: $x_i \to 1$; $\gamma_i \to 1$ $G^{ex}/RT \to 0$.

The adsorption of binary $CO_2(1)/CH_4(2)$ and $CH_4(1)/C_3H_8(2)$ mixtures in LTA-4A also exhibit thermodynamic non-idealities; see Figures S74–S77.

Use of Eq. (11), along with the fitted Wilson parameters $\Lambda_{12}, \Lambda_{21}, \Lambda_{13}, \Lambda_{31}, \Lambda_{23}, \Lambda_{32}$ for the three binary pairs (reported in Table S13), allows us to estimate the activity coefficients for ternary $CO_2/CH_4/C_3H_8$ mixtures in LTA-4A. For testing the accuracy of such estimations, CBMC simulations were carried out for 25/65/10 $CO_2/CH_4/C_3H_8$ mixtures in LTA-4A at 300 K for a range of total fugacities, f_t. In Fig. 8, the G^{ex}/RT determined from ternary CBMC data are plotted in 3D space as function of Φ and x_1. The continuous solid line represents the ternary RAST Wilson calculations. There is good agreement between the two sets, validating the ternary RAST Wilson model.

For adsorption of CO_2-bearing mixtures, CBMC simulations [38] show that the window regions of all-silica DDR and CHA zeolites have a significantly higher proportion of CO_2 than within the cages; see computational snapshots in Fig. 9. The resulting inhomogeneity in the

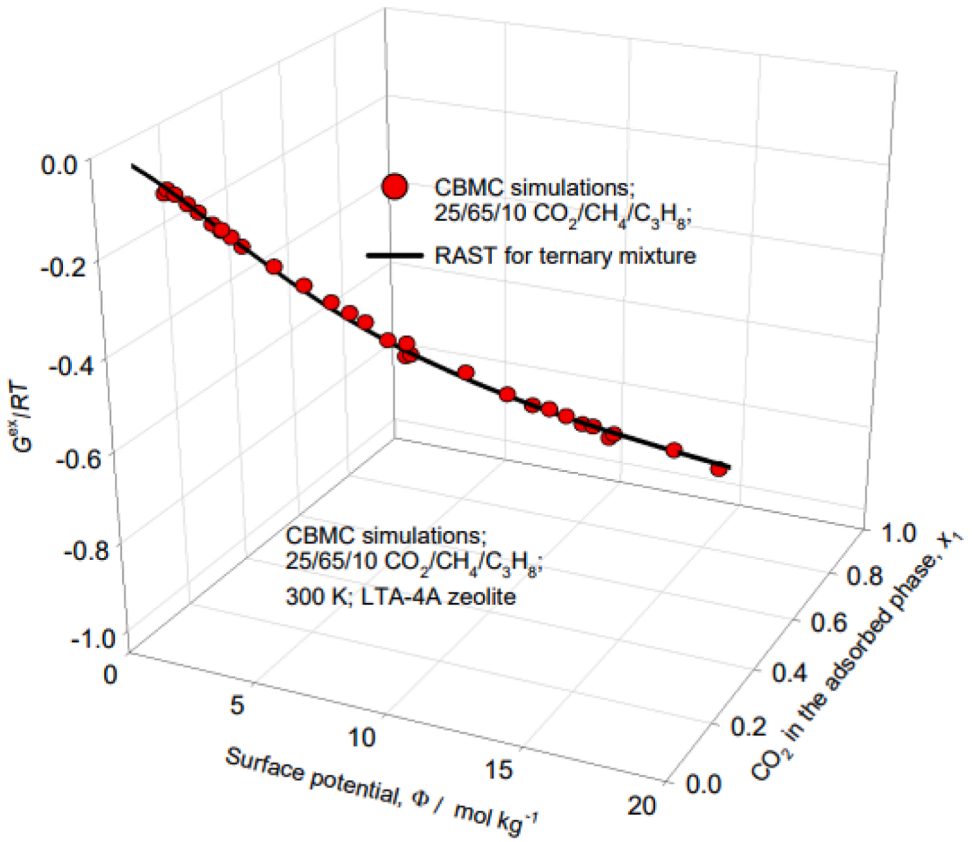

Fig. 8. 3D plot of CBMC data on excess Gibbs free energy G^{ex}/RT for 25/65/10 $CO_2(1)//CH_4(2)/C_3H_8(3)$ mixtures in LTA-4A zeolite at 300 K. Comparison is made with the estimates of the ternary Wilson RAST model. The Wilson parameters for the binary pairs are provided in Table S13. All simulation details are provided in the Supplementary Material accompanying this publication.

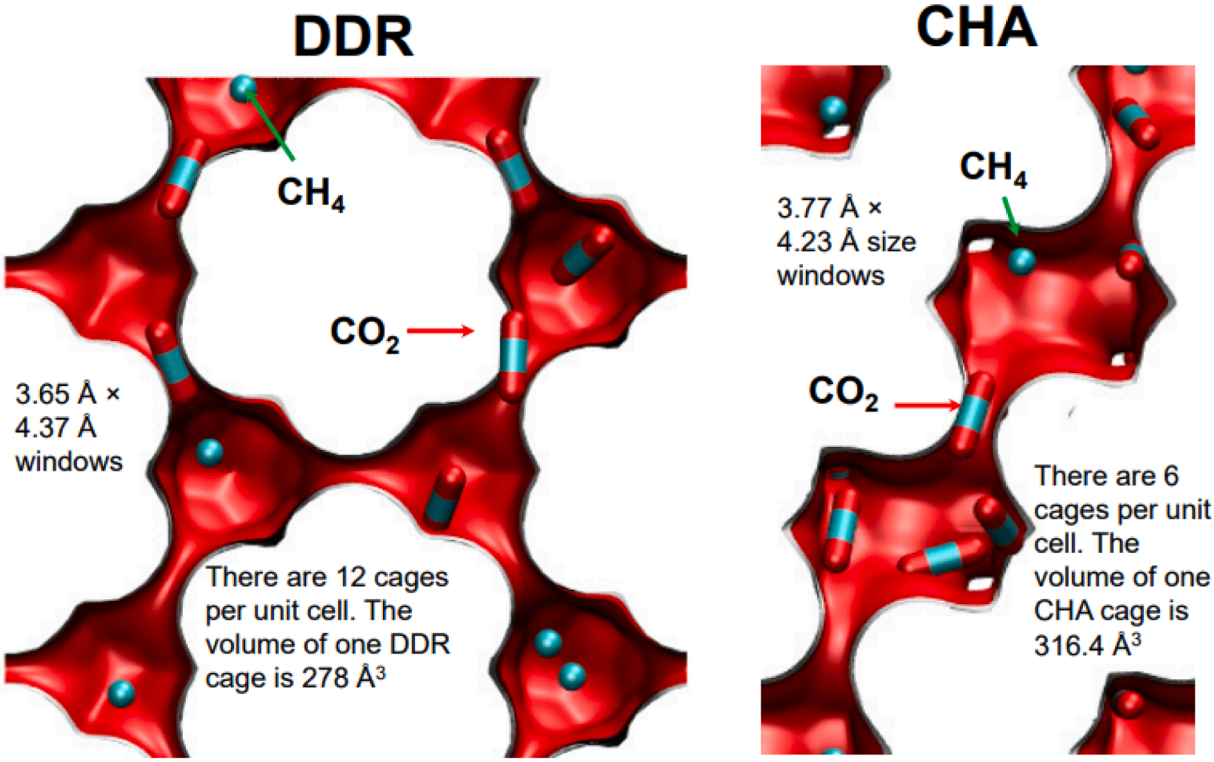

Fig. 9. Computational snapshots for $CO_2(1)/CH_4(2)$ mixture adsorption in (a) DDR, and (b) CHA zeolites at 300 K. All simulation details are provided in the Supplementary Material accompanying this publication.

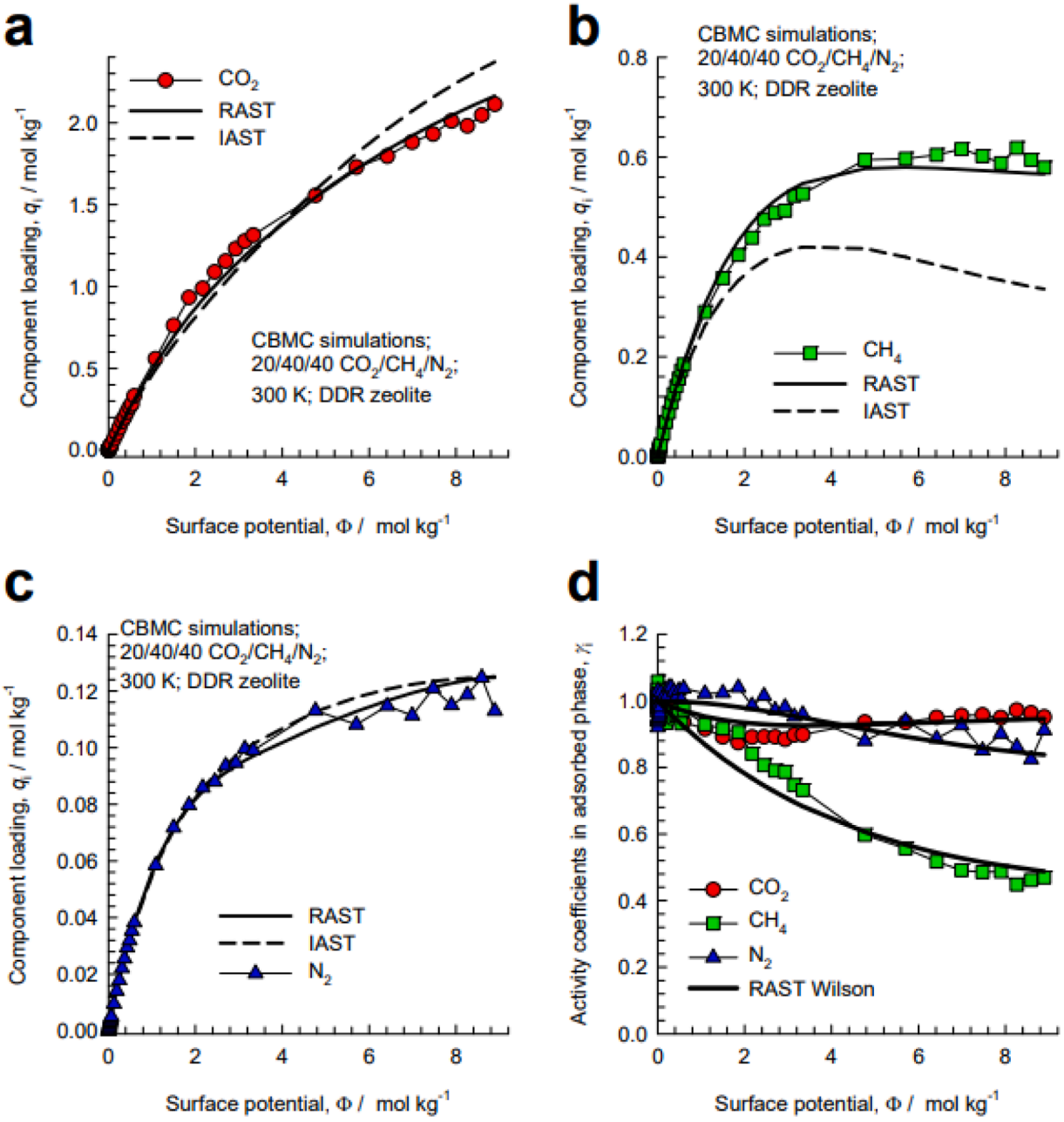

Fig. 10. CBMC simulations (indicated by symbols) for 20/40/40 $CO_2(1)//CH_4(2)/N_2(3)$ mixtures in DDR zeolite at 300 K. (a, b, c) Component loadings from CBMC are compared with IAST and RAST estimates. (d) Activity coefficients as function of the surface potential. The Wilson parameters for the binary pairs are provided in Table S8. All simulation details are provided in the Supplementary Material accompanying this publication.

distribution of guest adsorbates leads to deviations from the IAST; such deviations allow the rationalization and interpretation of membrane permeation data [8,38].

Fig. 10a–c present CBMC data for ternary 20/40/40 $CO_2/CH_4/N_2$ mixtures in DDR at 300 K for a range of total fugacities, f_t. The IAST estimates (indicated by the dashed lines) are not in good agreement with the CBMC data, especially for CH_4. The continuous solid lines are RAST calculations using Eq. (11) in which the Wilson parameters for the binary pairs Λ_{ij} are determined from fitting the non-idealites for the three constituent binary pairs; these are listed in Table S8. The RAST calculations are in good agreement with the CBMC data. Fig. 10d plots the component activity coefficients as function of the surface potential, Φ. Analogous data for adsorption of ternary 10/20/70 $CO_2/CH_4/H_2$ mixtures in DDR and CHA zeolites also confirm the estimation capability of Eq. (11); see Figures S14–S21, and S31–S38.

The preferential location of CO_2 in the side-pockets of MOR zeolite (see Figures S106–S112) and inhomogeneous of guest adsorbates for mixture adsorption rationalizes the deviations from thermodynamic idealities and selectivity reversals as witnessed in the experiments of Talu and Zwiebel [16] for CO_2/C_3H_8 mixtures in H-MOR. The

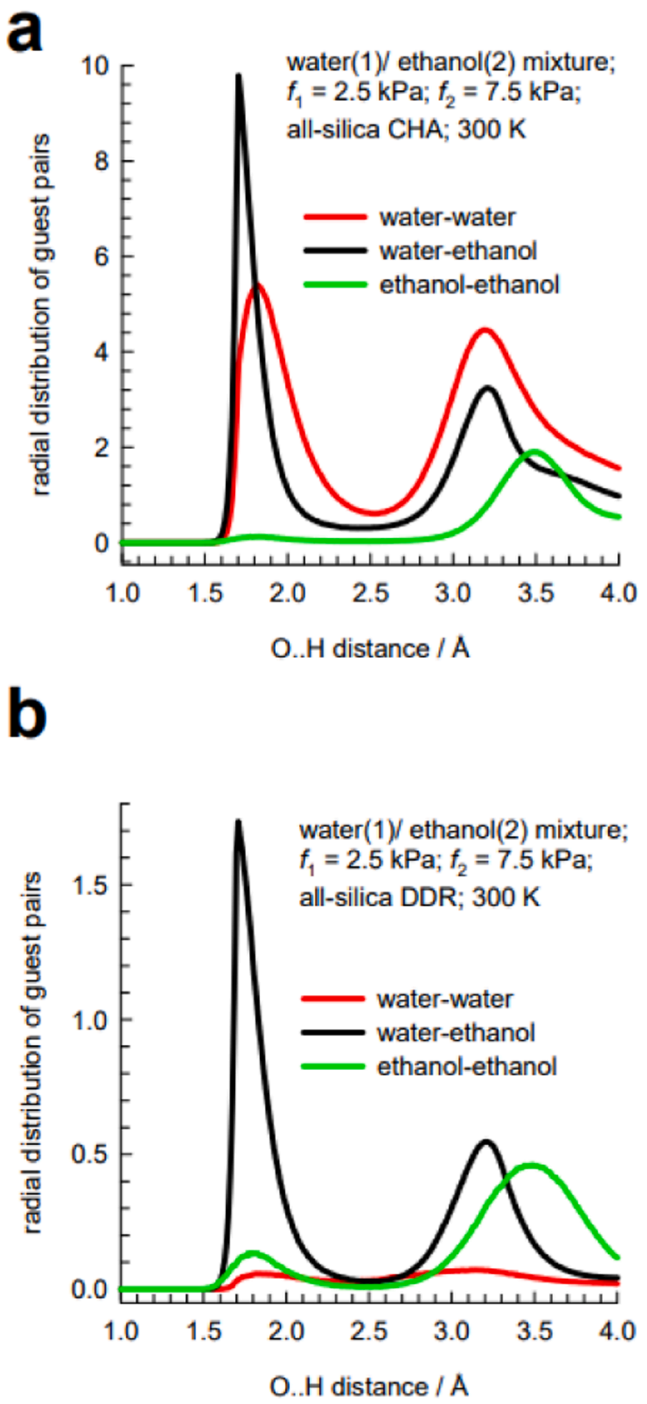

Fig. 11. RDF of O···H distances for molecular pairs of water(1)/ethanol(2) mixture adsorption in (a) DDR and (b) CHA zeolites at 300 K. The partial fugacities of components 1 and 2 are f_1= 2.5 kPa, f_2= 7.5 kPa. The magnitudes of the first peaks are a direct reflection of the degree of hydrogen bonding between the molecular pairs. All simulation details are provided in the Supplementary Material accompanying this publication.

experimental data presented in Figure S141b is in remarkable quantitative agreement with the corresponding CBMC simulations presented in Figure S111e.

3. Molecular clustering due to hydrogen bonding

For water/alcohol mixture adsorption, the manifestation of hydrogen bonding between water and alcohol molecules can be demonstrated by sampling the spatial locations of the guest molecules to determine the O···H distances of various pairs of molecular distances. For water(1)/ethanol(2) mixture adsorption in DDR and CHA zeolites at 300 K, the RDF of O···H distances for water-water, water-ethanol, and ethanol-ethanol pairs are shown in

Fig. 11. We note the first peaks in the RDFs occur at a distance <2 Å, that is characteristic of hydrogen bonding [45,46].The heights of the first peaks are a direct reflection of the degree of hydrogen bonding between the molecular pairs. The degree of H-bonding between water-ethanol pairs is significantly larger, by about an order of magnitude, than for water-water, and ethanol-ethanol pairs.

The occurrence of molecular clustering due to hydrogen bonding invalidates Eq. (7); this needs augmentation to include contribution due to the excess Gibbs energy as in Eq. (14). CBMC simulations for adsorption of water/methanol, water/ethanol, and methanol/ethanol mixtures in CHA, DDR, and MFI zeolites confirm the existence of strong non-idealities, see Figures S22-S29, S39-S46, and S90–S99. Consequently, CBMC data for equimolar $\left(f_1 = f_2 = f_3\right)$ water(1)/methanol(2)/ethanol(3) mixture adsorption in DDR zeolite also exhibits strong deviations from ideality as witnessed in Fig. 12 that plots $G^{ex}/RT = \sum_{i=1}^{n} x_i \ln(\gamma_i)$ in 3D space as function of the surface potential Φ and mole fraction of water(1) in the adsorbed phase mixture, x_1. The continuous solid line represents the ternary RAST NRTL calculations, following Eq. (13), using as inputs the fitted NRTL parameters for the constituent binary pairs. The agreement is good, validating the reliability of the ternary RAST NRTL model.

The proper accounting of thermodynamic non-idealities is necessary for understanding and interpreting experimental data on water/alcohol permeation across CHA, DDR, LTA, and ZIF-8 membranes [22-26].

4. Conclusions

The validity of the IAST mandates a homogeneous distribution of guest adsorbates in the pore space, without preferential location of any guest. CBMC data for adsorption of CO_2-bearing binary and ternary mixtures in cation-exchanged NaX zeolite show significant deviations from the IAST due to congregation of CO_2 around the extra-framework cations. The CO_2—CO_2 distances are significantly smaller than the distances of CO_2 from its partner(s). Due to the inhomogeneous distribution of adsorbates, the partner molecules endure reduced degree of competition with CO_2 than is presumed in the IAST. Consequently, the IAST generally tends to anticipate a higher selectivity of CO_2 with respect to partner species. The IAST also fails to anticipate reversals in selectivity of CO_2-bearing mixtures of varying composition.

In cage-type zeolites such as LTA-4A, CHA, and DDR that have narrow windows with apertures in the 3.6 Å–4.1 Å range, the preferential perching of CO_2 molecules at or near the window regions also causes the failure of the IAST due to segregtion of adsorbates, in much the same way as for NaX.

For adsorption of water/alcohol mixtures in CHA, DDR, and MFI zeolites, the formation of molecular clusters due to hydrogen bonding invalidates Eq. (7); this needs augmentation to include contribution due to the excess Gibbs energy as in Eq. (14).

The two major take-aways of this article are as follows. Firstly, the RAST modelling of the activity coefficients in the adsorbed phase mixtures requires us to consider the dependence on both the surface potential, Φ, and the mole fractions of adsorbates. Secondly, the adsorption equilibrium of ternary mixtures can be estimated with good accuracy using the fitted Wilson or NRTL parameters of the constituent binary pairs.

The modelling of transient breakthroughs in fixed bed adsorbers, and permeation fluxes across membrane permeation devices will require appropriate RAST models for mixture adsorption equilibrium [18,19,26-28,47].

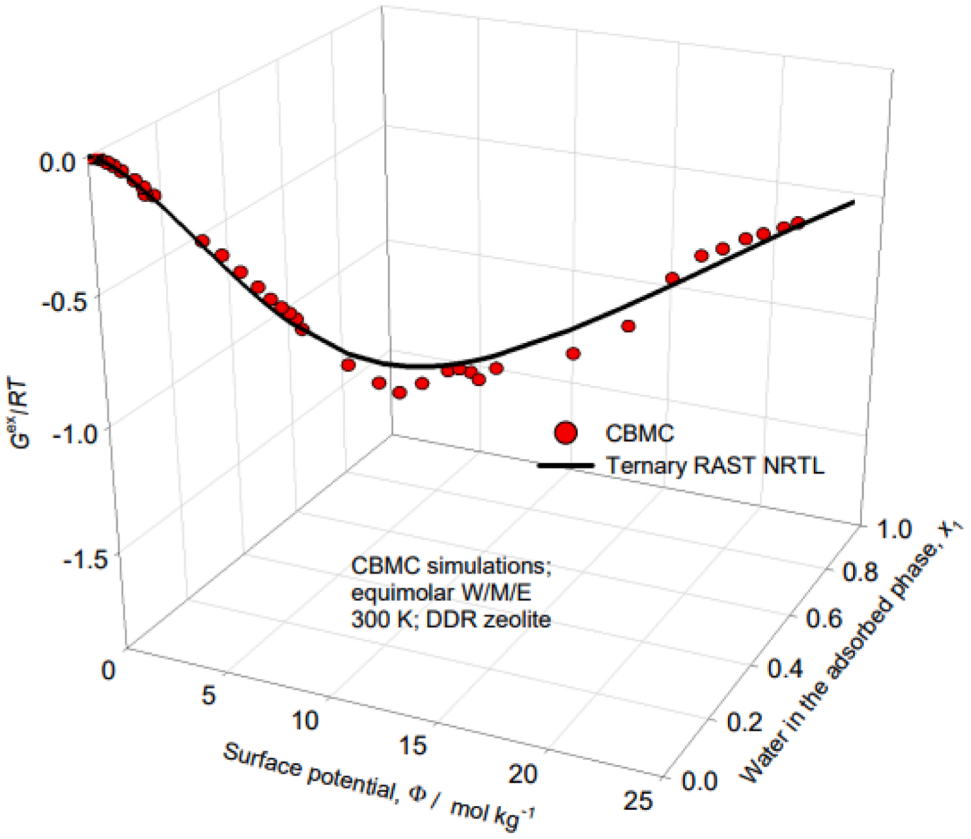

Fig. 12. 3D plot of CBMC data on excess Gibbs free energy $G^{ex}/RT = \sum_{i=1}^{n} x_i \ln(\gamma_i)$ for equimolar $(f_1 = f_2 = f_3)$ water(1)/methanol(2)/ethanol(3) mixtures in DDR zeolite at 300 K. Comparison is made with the estimates of the ternary NRTL RAST model. The NRTL parameters for the binary pairs are as provided in Table S9. All simulation details are provided in the Supplementary Material accompanying this publication.

CRediT authorship contribution statement

Rajamani Krishna: Writing – review & editing, Writing – original draft, Visualization, Validation, Supervision, Methodology, Investigation, Conceptualization. **Jasper M. van Baten:** Writing – review & editing, Validation, Software, Methodology, Conceptualization.

Declaration of competing interest

The authors declare no conflict of interests

Supplementary materials

Supplementary material associated with this article can be found, in the online version, at doi:10.1016/j.fluid.2024.114260.

Data availability

All data is provided in the Supplementary Material

References

[1] A.L. Myers, J.M. Prausnitz, Thermodynamics of mixed gas adsorption, AIChE J. 11 (1965) 121–130, https://doi.org/10.1002/aic.690110125.
[2] K.S. Walton, D.S. Sholl, Predicting multicomponent adsorption: 50 years of the ideal adsorbed solution theory, AIChE J. 61 (2015) 2757–2762, https://doi.org/10.1002/aic.14878.
[3] F.R. Siperstein, A.L. Myers, Mixed-gas adsorption, AIChE J. 47 (2001) 1141–1159, https://doi.org/10.1002/aic.690470520.
[4] A. Streb, M. Mazzotti, Adsorption for efficient low carbon hydrogen production: Part 1—Adsorption equilibrium and breakthrough studies for $H_2/CO_2/CH_4$ on zeolite 13X, Adsorption 27 (2021) 541–558, https://doi.org/10.1007/s10450-021-00306-y.
[5] O. Talu, A.L. Myers, Rigorous thermodynamic treatment of gas-adsorption, AIChE J. 34 (1988) 1887–1893.
[6] R. Krishna, Thermodynamic insights into the characteristics of unary and mixture permeances in microporous membranes, ACS Omega 4 (2019) 9512–9521, https://doi.org/10.1021/acsomega.9b00907.
[7] R. Krishna, J.M. Van Baten, Using molecular simulations to unravel the benefits of characterizing mixture permeation in microporous membranes in terms of the spreading pressure, ACS Omega 5 (2020) 32769–32780, https://doi.org/10.1021/acsomega.0c05269.
[8] R. Krishna, J.M. van Baten, Using the spreading pressure to inter-relate the characteristics of unary, binary and ternary mixture permeation across microporous membranes, J. Membr. Sci. 643 (2022) 120049, https://doi.org/10.1016/j.memsci.2021.120049.
[9] N.S. Wilkins, A. Rajendran, Measurement of competitive CO_2 and N_2 adsorption on zeolite 13X for post-combustion CO_2 capture, Adsorption 25 (2019) 115–133, https://doi.org/10.1007/s10450-018-00004-2.
[10] G. Avijegon, G. Xiao, G. Li, E.F. May, Binary and ternary adsorption equilibria for CO2/CH4/N2 mixtures on Zeolite 13X beads from 273 to 333 K and pressures to 900 kPa, Adsorption 24 (2018) 381–392, https://doi.org/10.1007/s10450-018-9952-3.
[11] F. Gholipour, M. Mofarahi, Adsorption equilibrium of methane and carbon dioxide on zeolite 13X: experimental and thermodynamic modeling, J. Supercrit. Fluids 111 (2016) 47–54.
[12] M. Hefti, D. Marx, L. Joss, M. Mazzotti, Adsorption equilibrium of binary mixtures of carbon dioxide and nitrogen on zeolites ZSM-5 and 13X, Microporous Mesoporous Mater. 215 (2015) 215–228.
[13] A. Streb, M. Mazzotti, Adsorption for efficient low carbon hydrogen production: part 2—Cyclic experiments and model predictions, Adsorption 27 (2021) 559–575, https://doi.org/10.1007/s10450-021-00308-w.
[14] E. Costa, G. Calleja, A. Jimenez, J. Pau, Adsorption equilibrium of ethylene, propane, propylene, carbon dioxide, and their mixtures in 13X zeolite, J. Chem. Eng. Data 36 (1991) 218–224, https://doi.org/10.1021/je00002a020.
[15] G. Calleja, J. Pau, J.A. Calles, Pure and multicomponent adsorption equilibrium of carbon dioxide, ethylene, and propane on ZSM-5 zeolites with different Si/Al ratios, J. Chem. Eng. Data 43 (1998) 994–1003.
[16] O. Talu, I. Zwiebel, Multicomponent adsorption equilibria of nonideal mixtures, AIChE J. 32 (1986) 1263–1276.
[17] D. Basmadjian, S.T. Hsieh, Isothermal column sorption of ethylene-carbon dioxide mixtures with azeotropic behaviour, Can. J. Chem. Eng. 58 (1980) 185–189, https://doi.org/10.1002/cjce.5450580208.

[18] I. van Zandvoort, E.-J. Ras, R. de Graaf, R. Krishna, Using transient breakthrough experiments for screening of adsorbents for separation of C_2H_4/CO_2 mixtures sep, Purif. Technol. 241 (2020) 116706, https://doi.org/10.1016/j.seppur.2020.116706.
[19] I. van Zandvoort, J.K. van der Waal, E.-J. Ras, R. de Graaf, R. Krishna, Highlighting non-idealities in C_2H_4/CO_2 mixture adsorption in 5A zeolite, Sep. Purif. Technol. 227 (2019) 115730, https://doi.org/10.1016/j.seppur.2019.115730.
[20] R. Krishna, J.M. Van Baten, Investigating the non-idealities in adsorption of CO_2-bearing mixtures in cation-exchanged zeolites, Sep. Purif. Technol. 206 (2018) 208–217, https://doi.org/10.1016/j.seppur.2018.06.009.
[21] S.H. Hyun, R.P. Danner, Equiilbrium adsorption of ethane, ethylene, isobutane, carbon dioxide, and their binary mixtures on 13X molecular sieves, J. Chem. Eng. Data 27 (1982) 196–200, https://doi.org/10.1021/je00028a029.
[22] J.Y. Wu, Q.L. Liu, Y. Xiong, A.M. Zhu, Y. Chen, Molecular simulation of water/alcohol mixtures adsorption and diffusion in zeolite 4A membranes, J. Phys. Chem. B 113 (2009) 4267–4274.
[23] S. Guo, C. Yua, X. Gua, W. Jin, J. Zhong, C.-J. Chen, Simulation of adsorption, diffusion, and permeability of water and ethanol in NaA zeolite membranes, J. Membr. Sci. 376 (2011) 40–49, https://doi.org/10.1016/j.memsci.2011.03.043.
[24] M. Pera-Titus, C. Fité, V. Sebastián, E. Lorente, J. Llorens, F. Cunill, Modeling pervaporation of ethanol/water mixtures within 'Real' zeolite NaA membranes, Ind. Eng. Chem. Res. 47 (2008) 3213–3224.
[25] B. Liu, H. Kita, K. Yogo, Preparation of Si-rich LTA membrane using organic template-free solution for methanol dehydration Sep, Purif. Technol. 239 (2020) 116533, https://doi.org/10.1016/j.seppur.2020.116533.
[26] R. Krishna, J.M. van Baten, Fundamental insights into the variety of factors that influence water/alcohol membrane permeation selectivity, J. Membr. Sci. 698 (2024) 122635, https://doi.org/10.1016/j.memsci.2024.122635.
[27] R. Krishna, J.M. Van Baten, Elucidating the failure of the ideal adsorbed solution theory for CO_2/H_2O mixture adsorption in CALF-20, Sep. Purif. Technol. 352 (2025) 128269, https://doi.org/10.1016/j.seppur.2024.128269.
[28] R. Krishna, J.M. van Baten, Non-Idealities in adsorption thermodynamics for CO_2 capture from humid natural gas using CALF-20, Sep. Purif. Technol. 355 (Part A) (2025) 129553, https://doi.org/10.1016/j.seppur.2024.129553.
[29] S. Sochard, N. Fernandes, J.-M. Reneaume, Modeling of adsorption isotherm of a binary mixture with real adsorbed solution theory and nonrandom two-liquid model, AIChE J. 56 (2010) 3109–3119, https://doi.org/10.1002/aic.12220.
[30] N. Mittal, P. Bai, I. Siepmann, P. Daoutidis, M. Tsapatsis, Bioethanol enrichment using zeolite membranes: molecular modeling, conceptual process design and techno-economic analysis, J. Membr. Sci. 540 (2017) 464–476.
[31] G. Calleja, A. Jimenez, J. Pau, L. Domínguez, P. Pérez, Multicomponent adsorption equilibrium of ethylene, propane, propylene and CO_2 on 13X zeolite, Gas Sep. Purif. 8 (1994) 247–256, https://doi.org/10.1016/0950-4214(94)80005-7.
[32] H. Kaur, B.D. Marshall, Real adsorbed solution theory model for the adsorption of CO_2 from humid gas on CALF-20, ChemRxiv (2023) 1–18, https://doi.org/10.26434/chemrxiv-2023-2cp2c.
[33] T.J.H. Vlugt, R. Krishna, B. Smit, Molecular simulations of adsorption isotherms for linear and branched alkanes and their mixtures in silicalite, J. Phys. Chem. B 103 (1999) 1102–1118, https://doi.org/10.1021/jp982736c.
[34] D. Dubbeldam, R. Krishna, S. Calero, A.Ö. Yazaydın, Computer-assisted screening of ordered crystalline nanoporous adsorbents for separation of alkane isomers, Angew. Chem. Int. Ed. 51 (2012) 11867–11871, https://doi.org/10.1002/anie.201205040.
[35] D. Dubbeldam, S. Calero, T.J.H. Vlugt, R. Krishna, T.L.M. Maesen, B. Smit, United atom forcefield for alkanes in nanoporous materials, J. Phys. Chem. B 108 (2004) 12301–12313.
[36] R. Krishna, J.M. van Baten, Maxwell-Stefan modeling of slowing-down effects in mixed gas permeation across porous membranes, J. Membr. Sci. 383 (2011) 289–300, https://doi.org/10.1016/j.memsci.2011.08.067.
[37] R. Krishna, J.M. van Baten, Investigating the influence of diffusional coupling on mixture permeation across, Porous Membr. J. Membr. Sci. 430 (2013) 113–128, https://doi.org/10.1016/j.memsci.2012.12.004.
[38] R. Krishna, J.M. van Baten, Segregation effects in adsorption of CO_2 containing mixtures and their consequences for separation selectivities in cage-type zeolites, Sep. Purif. Technol. 61 (2008) 414–423, https://doi.org/10.1016/j.seppur.2007.12.003.
[39] R. Krishna, J.M. van Baten, Onsager coefficients for binary mixture diffusion in nanopores, Chem. Eng. Sci. 63 (2008) 3120–3140.
[40] R. Krishna, J.M. van Baten, In silico screening of zeolite membranes for CO_2 capture, J. Membr. Sci. 360 (2010) 323–333, https://doi.org/10.1016/j.memsci.2010.05.032.
[41] R. Krishna, J.M. van Baten, A comparison of the CO_2 capture characteristics of zeolites and metal-organic frameworks, Sep. Purif. Technol. 87 (2012) 120–126, https://doi.org/10.1016/j.seppur.2011.11.031.
[42] R. Krishna, J.M. Van Baten, Elucidation of selectivity reversals for binary mixture adsorption in microporous adsorbents, ACS Omega 5 (2020) 9031–9040, https://doi.org/10.1021/acsomega.0c01051.
[43] R. Krishna, J.M. Van Baten, Using molecular simulations for elucidation of thermodynamic non-idealities in adsorption of CO_2-containing mixtures in NaX zeolite, ACS Omega 5 (2020) 20535–20542, https://doi.org/10.1021/acsomega.0c02730.
[44] R. Krishna, J.M. Van Baten, How reliable is the ideal adsorbed solution theory for estimation of mixture separation selectivities in microporous crystalline adsorbents? ACS Omega 6 (2021) 15499–15513, https://doi.org/10.1021/acsomega.1c02136.
[45] C. Zhang, X. Yang, Molecular dynamics simulation of ethanol/water mixtures for structure and diffusion properties, Fluid Phase Equilib. 231 (2005) 1–10, https://doi.org/10.1016/j.fluid.2005.03.018.
[46] R. Krishna, J.M. van Baten, Hydrogen bonding effects in adsorption of water-alcohol mixtures in zeolites and the consequences for the characteristics of the Maxwell-Stefan diffusivities, Langmuir 26 (2010) 10854–10867, https://doi.org/10.1021/la100737c.
[47] R. Krishna, J.M. van Baten, R. Baur, Highlighting the origins and consequences of thermodynamic non-idealities in mixture separations using zeolites and metal-organic frameworks, Microporous Mesoporous Mater. 267 (2018) 274–292, https://doi.org/10.1016/j.micromeso.2018.03.013.